Spin Crossover Induced By Changing the Identity Of the Secondary Metal Species In A Face-Centred $Fe^{II}_8Ni^{II}_6$ Cubic Cage

*Hyunsung Min, Alexander R. Craze†, Matthew J. Wallis, Ryuya Tokunaga, Takahiro Taira, Yutaka Hirai, Mohan M. Bhadbhade, Daniel J. Fanna, Christopher E. Marjo, Shinya Hayami, Leonard F. Lindoy and Feng Li**

Hyunsung Min, Matthew J. Wallis, Alexander R. Craze, Daniel J. Fanna, Feng Li - School of Science, Western Sydney University, Locked Bag 1797, Penrith NSW 2751, Australia

Alexander R. Craze - Department of Chemistry, University of Oxford, 12 Mansfield Road, Oxford OX1 3TA, UK (current address)

Ryuya Tokunaga, Takahiro Taira, Yutaka Hirai, Shinya Hayami Department of Chemistry, Graduate School of Science and Technology, Kumamoto University, 2-39-1 Kurokami, Chuo-ku, Kumamoto 860-8555, Japan.

Mohan M. Bhadbhade, Christopher E. Marjo - Mark Wainwright Analytical Centre, University of New South Wales, Kensington, NSW, 2052, Australia

Leonard F. Lindoy - School of Chemistry, University of Sydney, Camperdown, NSW 2006, Australia

ABSTRACT

The assembly of multifunctional polynuclear coordination cages exhibiting spin-crossover (SCO) proves to be a challenge to researchers. Previous investigations into the magnetic properties of a large cubic metallosupramolecular cage, $[Fe_8Pd_6\mathbf{L}_8]^{28+}$, constructed using semi-rigid metalloligands and encompassing an internal void of 41 $Å^3$, found that the Fe(II) centres that occupied the corners of the cubic structure did not undergo a spin-transition. In this work, substitution of the linker metal on the face of the cage resulted in the onset of spin crossover, as evidenced by magnetic susceptibility, Mössbauer and single crystal X-ray diffraction. Structural comparisons of these two cages were undertaken to shed light on the possible mechanism responsible for switching of the $[Fe_8M(II)_6\mathbf{L}_8]^{28+}$ architecture from SCO inactive to active by simply changing in the identity of M(II). This led to the suggestion that a possible interplay of intra- and intermolecular interactions may permit SCO in the Ni(II) analogue, **1**. The distorted octahedral coordination environment of the secondary Ni(II) centres occupying the cage faces provided conformational flexibility for the eight metalloligands of the cubic architecture relative to the square planar Pd(II) environment. Meanwhile the occupation of axial coordination sites of the Ni(II) cations by CH_3CN prevented the close packing of cages observed for the Pd(II) analogue, leading to a more offset, distant packing arrangement of cages in the lattice, whereby important areas of the cage that were shown to change most dramatically with SCO experienced a lesser degree of steric hindrance to conformational changes upon SCO. Design through selectivity of secondary metal centres on the flexibility of metalloligand structures and the effect of axial donors

packing arrangements may serve as new routes in the engineering of SCO or non-SCO cage systems.

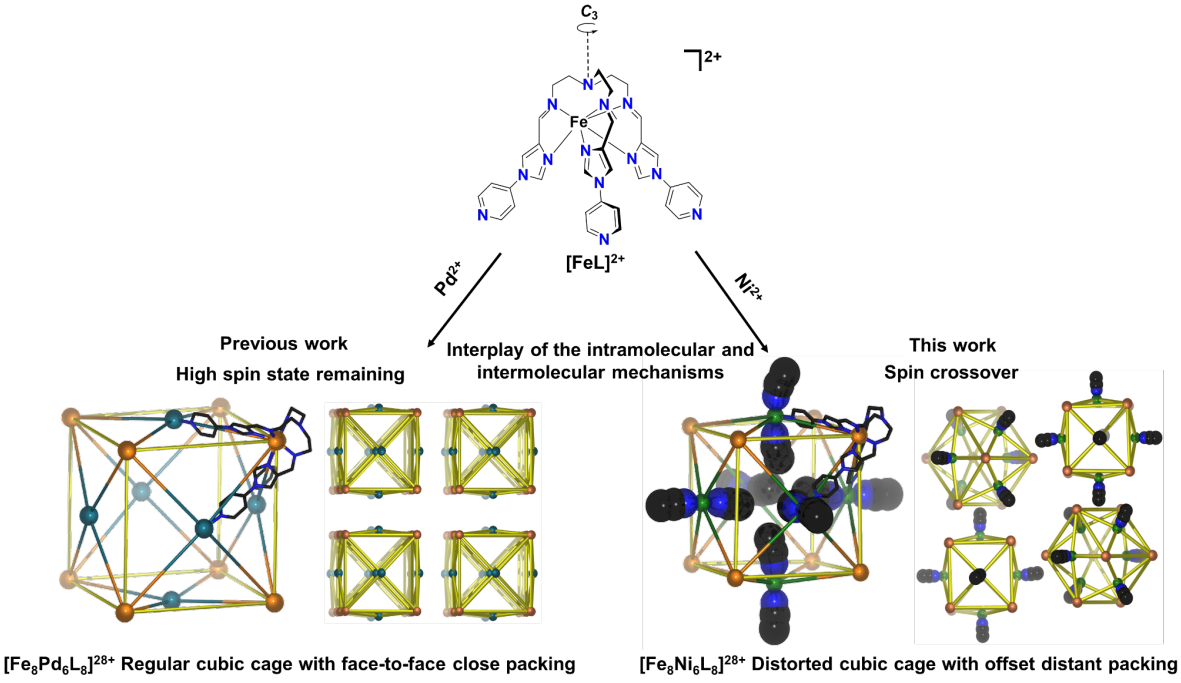

INTRODUCTION

The design and assembly of discrete polynuclear materials that incorporate an internal cavity remains an active goal in metallo-supramolecular chemistry.[1,2] Such molecules have shown potential in a range of future applications which take advantage of host-guest interactions, including sensing,[3-6] catalysis,[7-10] drug encapulation[11,12] and the selective uptake of guest molecules[13-16]. In addition, there has been continuing interest in the construction of new cage systems as photoactive[17-19] and magnetic materials,[20] with the latter including spin crossover (SCO) systems.[21-42] Currently, there exists a vast structural diversity of metallo-organic cages, owing to the development of multiple synthetic strategies that frequently involve metal-directed self-assembly.[1,2,43-45] One widely employed strategy is the metalloligand approach.[23,46-54] Variation of the nature of metal ions and ligand scaffold can direct cage assembly, and has resulted in the generation of a variety of cage topologies, motivated by the search for increased functionality and complexity[55]. Consequently, interest in heterometallic cage systems has greatly increased over recent years as a result of the potential for multifunctionality.[20]

Spin crossover (SCO) behaviour has largely been reported for homometallic cages,[21-22,24-27,34-37,41] with reports of heterometallic SCO systems being relatively rare.[23,38-40] The majority of SCO systems reported for coordination cages demonstrate gradual and incomplete spin-transitions[21-27,34-42] (ST) with only a few demonstrating complete spin transition.[22,36] Upon SCO, the coordination of the active metal centre must be able to undergo a significant conformational change. In large polynuclear cages, take cubic cages for instance, for complete SCO to occur, eight metal centres must undergo SCO. As such, these architectures must have the capacity for such large conformational changes to occur in the coordination environment of all eight SCO sites. This places a severe intramolecular steric strain on the cage architecture, and unless the conformational

changes required are cooperative, these strains may inhibit the ability of some metal centres to undergo SCO. For those cages that do exhibit a complete (or near enough to) SCO, the ligand scaffold consists of more flexible linkers, providing the necessary conformational freedom to compensate for the changes in coordination environments.[36,41] Conversely, in the cases of cages constructed from rigid ligand building blocks — which are more commonly used, as these provide more control over the binding geometry and supramolecular architecture — complete SCO is less frequently observed.[23,38,42]

One popular design of heterometallic coordination cages with SCO properties is the cubic architecture that possesses eight metals (often Fe(II)) in the corner positions and six metals occupying the faces (See Figure 1).[23,38] This is a promising design as it allows further control of the supramolecular architecture, using the binding mode and affinity of primary and secondary metals, and for the possibilities of extra functionality with two different metal types, positions and coordination environments.[23,34,,38-40] Although, this design strategy can be problematic for SCO, as the secondary facial bridging metal can place further steric restrictions on the SCO metallogliand corners by locking in the pendant arms. This is complicated further in the solid state, whereby another factor complicating the ST in large polynuclear supramolecular architectures is the close packing that can occur, which may further hinder the large distortions required of the metalloligand scaffold for SCO to occur.

Recently, we presented an $[Fe_8Pd_6\mathbf{L}_8]^{28+}$ tetradecanuclear cubic cage,[47] utilising the semi-rigid HS tripodal metalloligand ($[Fe\mathbf{L}](BF_4)_2$**)** shown below in Figure 1 to coordinate six Pd(II) centres in the faces of a cubic cage, demonstrating close face-to-face packing of the cages structures in the solid-state. This structure remained high spin at the Fe(II) centres even to low temperatures, with no SCO observed. In this study, we present an analogous structure, that differs in the identity of

the facial bridging metal, in this case Ni(II), forming a $[Fe_8Ni_6\mathbf{L}_8(CH_3CN)_{12}]^{28+}$ heterometallic cubic cage, (**1**). Remarkably, simply by changing the identity of the square planar four coordinate Pd(II) to the distorted octahedral six coordinate Ni(II) metal centre, complete and incomplete SCO was observed through crystallographic and magnetic susceptibility measurements respectively, owing to the degree of solvation. The emergence of SCO behaviour of the corner occupying Fe(II) species could be the result of three possible changes to the solid-state material. Firstly, the change could arise from the electronic environment of the Ni(II) affecting the Fe(II) centres via the conjugated metalloligand backbone. Secondly, it could be intramolecular, whereby the distorted octahedral Ni(II) occupying the faces provides the metalloligand scaffold with greater potential to conform with SCO in the Fe(II) centres. Lastly, the addition of acetonitriles that occupy the axial Ni(II) positions were found to promote packing of the cages in an offset packing arrangement with larger void spaces, in contrast to the closely packed $[Fe_8Pd_6\mathbf{L}_8]^{28+}$ HS analogue, which may again enhance the capability to conform with SCO. Alternatively it could be a combination of these mechanisms. Herein we explore the synthesis of **1** via the metalloligand approach, the characterization by magnetic, variable temperature single crystal X-ray diffraction (VT-SCXRD), CHN analysis, scanning electron microscopy-energy-dispersive spectroscopy (SEM-EDS), thermal gravimetric analysis and differential scanning calorimetry (TGA-DSC) and ultra-violet visible spectroscopy (UV-Vis). Furthermore the magnetostructural correlations are explored to elucidate the possible mechanism by which the $Fe_8M(II)_6\mathbf{L}_8$ architecture may switch from SCO inactive to SCO active with the facile change in the identity of M(II) from Pd(II) to Ni(II).

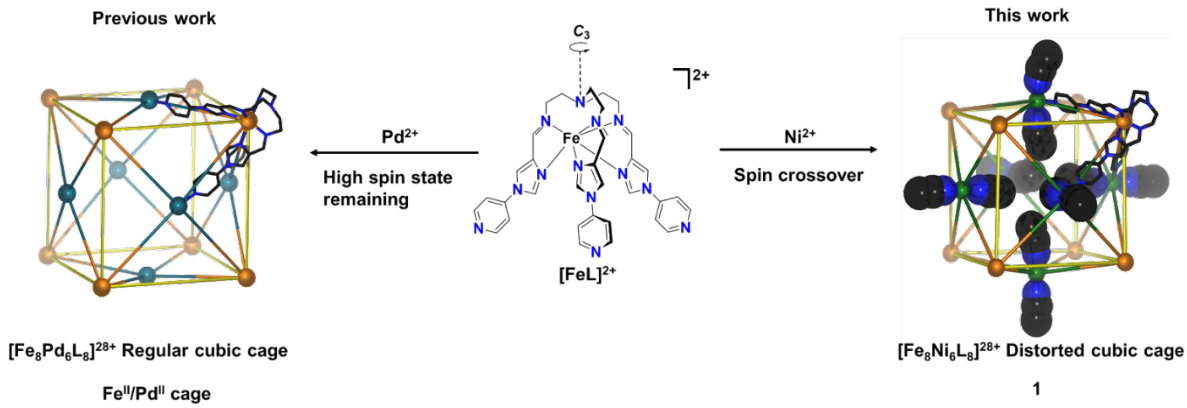

Figure 1. Schematic representation of the synthesis of a SCO inactive $[Fe_8Pd_6\mathbf{L}_8]^{28+}$ cage and its $[Fe_8Ni_6\mathbf{L}_8]^{28+}$ analogue, **1**, from the metalloligand $[Fe\mathbf{L}](BF_4)_2$.

Results and Discussion

*Synthesis and Characterisation of **1***

The HS Fe(II) metalloligand $[Fe\mathbf{L}](BF_4)_2$ was prepared by the reported method.[47] Self-assembly of the heterobimetallic cage **1** was carried out by the addition of $Ni(BF_4)_2$ to a solution of $[Fe\mathbf{L}](BF_4)_2$ in acetonitrile in a 4:3 stoichiometric ratio. Slow vapour diffusion of di-isopropyl ether into the reaction mixture in acetonitrile (CH_3CN) yielded dark orange/red block crystals (Figure S1). The crystals were filtered and air dried to give 57.0% yield of **1,** which has been fully characterised by CHN, SEM-EDS, VT-SCXRD, TGA-DSC and UV-Vis spectroscopy. The SEM images of **1** demonstrate the trapezoidal morphology of **1** and the decay upon losing solvent. Moreover EDS analysis confirmed the presence of C, N, F, Fe and Ni and the ratio of Fe(II) to Ni(II) in the cage to be approximately 4:3 (Figure S2). The element maps of **1** demonstrates that each element was uniformly distributed throughout the crystal, showing chemical homogeneity (Figure S2). A mass loss -7.46 % was observed in TGA experiments (Figure S3), which also

showed **1** starts to decompose from 610.2 K (Figure S3). Similarly, STA measurements demonstrate the presence of similar amounts of solvent molecules in the crystalline sample of **1**.

Single Crystal X-ray Diffraction

Variable-temperature Single crystal X-ray diffraction experiments were conducted on a dark orange/red block crystal at 100, 150, 200, 250 and 275 K. The X-ray structure confirmed the formation of a heterodinuclear cubic cage **1** (Figure 2), which crystallised in the monoclinic space group $P2_1/c$ (Table S1 in S2 of the ESI). The asymmetric unit at 100 K consists of one complete cage, with five disordered tetrafluoroborate anions resolved, both within and outside the internal cage cavity. As the temperature of the measurements were increased, thermally induced disorder meant the number of tetrafluoroborate (BF_4^-) anions that were able to be resolved decreased, until at 275 K where no anions were resolved. Furthermore, **1** exhibits both possible homochiral enantiomers (Δ and Λ) with all $[Fe\mathbf{L}]^{2+}$ metalloligand centers of the cage being in either the $\Lambda\,\Lambda\,\Lambda\,\Lambda\,\Lambda\,\Lambda\,\Lambda\,\Lambda$ or $\Delta\,\Delta\,\Delta\,\Delta\,\Delta\,\Delta\,\Delta\,\Delta$ configuration in the asymmetric unit. Each secondary Ni(II) metal centre coordinates equatorially with four distal pyridyl nitrogens of four different metalloligands to form a pseudo fourfold symmetry axes of the cubic cage, with two nitrogens from CH_3CN in the axial positions to form a distorted octahedral coordination environment (Figure 2).

The average Fe-$N_{imidazolimine}$ bond lengths (2.17 at 275 K and 1.97 Å at 100 K) and average octahedral distortion (Σ) values (104.7˚ at 275 K and 55.0˚ at 100K) of **1** are in accord with HS and LS values at 275 and 100 K respectively (Table 1). The plots of both the average Fe-$N_{imidazolimine}$ bond lengths and the Fe-$N_{imidazolimine}$ bond lengths of each of the eight Fe(II) centres of the **1** as a function of temperature (in Figure 3) show a sigmoidal behaviour indicative of SCO in all Fe(II) centres.

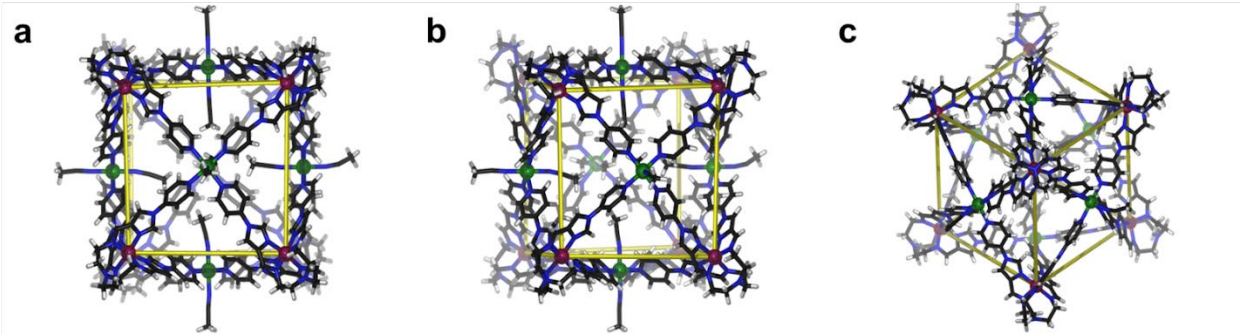

Figure 2. SCXRD structure of **1** at 100 K, shown a) down the pseudo C_4 axis, b) in an offset view and c) down the pseudo C_3 axis. The BF_4^- anions and solvent molecules are omitted for clarity (Fe, purple; Ni, green; C, black; N, blue; H, white).

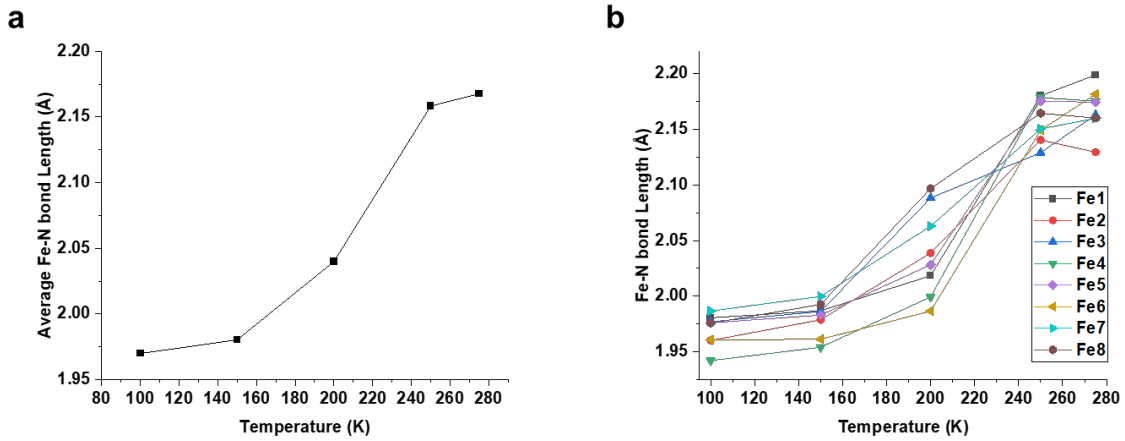

Figure 3. Plots of a) average Fe-N bond lengths and b) individual Fe-N bond lengths for each of the eight Fe(II) centres of **1** as a function of temperature.

Other crystallographic parameters such as the average total difference of all coordination bond lengths (ζ) and average total trigonal projection distortion parameter (Θ) were also calculated. These values were demonstrated to be 0.10 and 0.25Å (ζ) and 180.9 and 269.5˚ (Θ) respectively at 100 and 275 K. The octahedral distortion parameters describing the average coordinate bond length and the angular parameters representing the sum of deviations of each octahedral cis bond from 90° (Σ) and the sum of deviations from 60° of the cis bonds as projected in a plane orthogonal

to the pseudo-threefold axes of the octahedron (Θ) were calculated using OctaDist[56] to gauge the spin state at each Fe(II) center.

Table 1. Various crystallographic parameters of **1**, the previously reported $[Fe_8Pd_6\mathbf{L}_8]^{28+}$ cage and $[Fe\mathbf{L}](BF_4)_2$,[47] obtained through variable temperature single crystal X-ray diffraction.

Compound	Average Fe-N Bond Length (Å)	Σ (˚)	Θ (˚)	Fe···Fe Distance (Å)[a]	M···M Distance (M = Ni, Pd) (Å)[b]	Crystal Packing Coefficient (%)
1 (100 K)	1.97	55.0	180.9	24.86	17.25	28.7
1 (150 K)	1.98	57.5	190.6	24.90	17.29	28.3
1 (200 K)	2.04	69.2	216.3	24.90	17.17	27.9
1 (250 K)	2.16	105.3	279.4	25.65	16.98	26.6
1 (275 K)	2.17	104.2	269.5	25.57	16.80	27.0
$[Fe\mathbf{L}](BF_4)_2$ (100 K)	2.20	105.0	280.4	N/A	N/A	54.6
$[Fe_8Pd_6\mathbf{L}_8]^{28+}$ (100 K)	2.19	131.3	374.1	25.21	16.30	33.4

[a] Intramoleuclar Fe···Fe distance along pseudo three-fold symmetry axis.[b] Intramoleuclar M···M distance along pseudo four-fold symmetry axis (M = Ni and Pd).

Magnetic Susceptibility

The magnetic susceptibility experiments were conducted on solvated and desolvated samples of **1**, with LIESST experiments being conducted on the solvated sample only. The solvated materials

exhibited a gradual, two-step and incomplete spin transition (Figure 3a and S4) over the temperature range of 50-400 K. At 400 K a $\chi_m T$ of 34.64 cm^3 K mol^{-1} corresponds to all eight Fe(II) centres in the HS configuration, as well as six non-interacting paramagnetic Ni(II) centres.[57] The gradual decrease in susceptibility was observed to possess two $T_{1/2}$ values of 325 and 192 K (Figure S4). The susceptibility then plateaued at 50 K at 24.19 cm^3 K mol^{-1}, representative of three Fe(II) centres having transitioned to the LS state. The susceptibility was then observed to fall off sharply due to zero field splitting in residual paramagnetic Fe(II) and Ni(II) at low temperatures. To test for scan rate dependencies, the sample was then cycled at 1 and 4 K min^{-1}, and both were consistent (Section S4 of the ESI).

Next, to examine the effect of solvent loss, after successive heating and cooling cycles solvated **1** was held at 400 K for a 60-minute isotherm to induce loss of solvent. The magnetic susceptibility of desolvated **1** at 4 K min^{-1} demonstrated a similar gradual, two-step incomplete spin transition (Figure 3a and S4), with similar $\chi_m T$ values from 300 to 400 K, although with a consistently higher $\chi_m T$ value from 300 to 400 K compared to solvated **1** (Figure 3a). The $\chi_m T$ values of desolvated **1** closely matched that of the solvated sample at 400 K, which from 34.59 cm^3 K mol^{-1} decreased with $T_{1/2}$ values of 150 and 352 K (Figure S4) to a plateau value of 25 cm^3 K mol^{-1} at 52 K. This indicates that desolvation of the material results in more residual HS Fe(II) centres remaining at low temperatures. This may explain the discrepancy between single crystal and magnetic susceptibility measurements, as the samples were prone to desolvation (See Figure S2 of the ESI).

LIESST experiments were conducted for solvated samples of **1** to determine the photoexcitation response to red (800 nm) and green light (532 nm). **1** displayed a photomagnetic response for both red and green light sources on irradiation at 5 K (Figure 3b). Upon heating of the sample following photoexcitation with the green laser, the $\chi_m T$ value continues to increase until 28.73 cm^3 K mol^{-1}

at 57 K, with a T_{LIESST} value of 77 K, after which it begins to fall off. Similarly, excitation under red light provoked a similar response, with a slightly larger increase in the $\chi_m T$ value to 29.67 cm^3 K mol^{-1} at 47 K. For both photoexcited samples, the behaviour of the samples beyond the critical temperature are similar to each other, aligning well with the solvated 4 K heating curve.

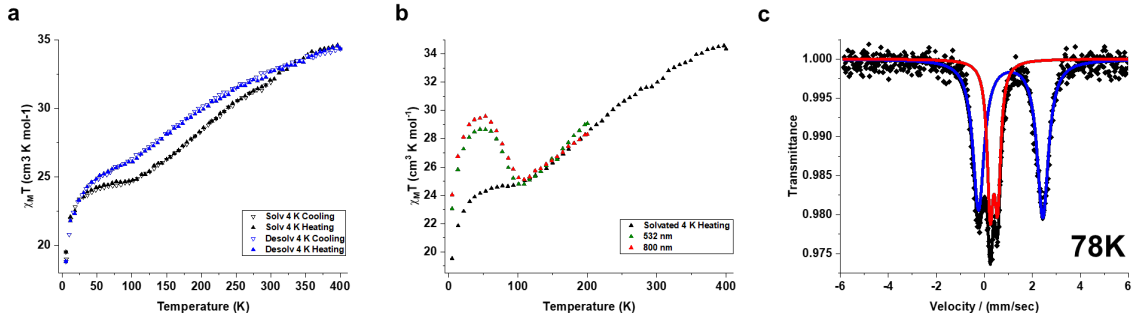

Figure 3. a) χ_mT *versus T* plot for solvated and desolvated **1** at scan rates of 4 K min^{-1}. b) Plot of LIESST experiments for solvated **1** with reference to 4 K min^{-1} heating cycle. c) Mössbauer spectra of solvated **1** at 78 K. The Fe(II) HS shown in blue and LS shown in red.

The Mössbauer experiment at 78 K for the solvated **1** supports the existence of both HS and LS Fe(II) centres. Two quadrupole-split doublets are identified (Figure 3c), the first doublet is wide (quadrupole-splitting Q.S. – 2.67 mm s^{-1} and an isomer shift I.S. = 1.09 mm s^{-1}), whereas the second doublet is narrow (Q.S. = 0.31 mm s^{-1} and I.S. = 0.40 mm s^{-1}), which represents the HS and LS states respectively. The area ratios of the Mössbauer absorption intensities of the HS and LS species (68:32) are in agreement with the $\chi_m T$ value of the magnetic susceptibility data (Section S4 of the ESI), suggesting that the incomplete spin transition arises from three of the eight Fe(II) metal centres changing from HS to LS.

Magneto-structural Correlations

In order to investigate possible causes of the sudden onset of SCO with the addition of the Ni(II) species to the cage faces, replacing Pd(II), a variety of intra- and intermolecular structural parameters were compared between the metalloligand, the $[Fe_8Pd_6\mathbf{L}_8]^{28+}$ cage that did not undergo SCO, and it's Ni(II) analogue **1** that was SCO active. Firstly, the intramolecular parameters will be described, followed by examination of intermolecular and packing effects. A variety of structural parameters are presented in Table 1, and these demonstrate the various structural conformations that the metalloligands must undergo when coordinating the secondary metal ion and forming these cage architectures. The HS state was found to be fully occupied in the structures of $[Fe\mathbf{L}](BF_4)_2$, $[Fe_8Pd_6\mathbf{L}_8]^{28+}$ and the 275 K structure of **1**. The HS Fe-$N_{imidazolimine}$ bond lengths for the three structures all showed very similar values between 2.17 and 2.20 Å. Analysis of the angular parameters Σ and Θ suggests that the Fe(II) coordination environment of the metalloligand must distort much more severely from a perfect octahedron in the $[Fe_8Pd_6\mathbf{L}_8]^{28+}$ structure, with Σ and Θ values of 131.3 and 374.1˚, compared to much smaller values of 105.0 and 280.4˚ for the metalloligand and 104.2 and 269.5˚ for **1**. In other words, the Fe(II) coordination environment of the metalloligand must severely distort when forming $[Fe_8Pd_6\mathbf{L}_8]^{28+}$, while in **1**, the coordination environment remains similar to that of the metalloligand. This large distortion of the Fe(II) coordination centre in the $[Fe_8Pd_6\mathbf{L}_8]^{28+}$ structure may cause a large degree of intramolecular strain throughout the cage, and play a role in this structure remaining HS at low temperatures by increasing energetic barriers to reorganisation of the ligand field required for SCO. Furthermore, occupation of antibonding orbitals by the axial acetonitrile donors, as well as their π-acceptor ability may reduce the Ni-$N_{pyridine}$ bond order and allow the flexibility required of the coordination environment upon SCO.

Table 2. Secondary bonding axes and ligand torsion angle for **1**, $[Fe_8Pd_6\mathbf{L}_8]^{28+}$ and $[Fe\mathbf{L}](BF_4)_2$.[47]

Compound	Secondary Bonding Axes (˚)	Ligand Torsion Angle (˚)
1 (100 K)	64.0	63.2
1 (150 K)	64.0	62.9
1 (200 K)	63.0	59.1
1 (250 K)	60.8	54.8
1 (275 K)	61.1	55.4
$[Fe\mathbf{L}](BF_4)_2$ (100 K)	55.3	50.1
$[Fe_8Pd_6\mathbf{L}_8]^{28+}$ (100 K)	61.3	55.4

In order to identify the extent of the metalloligand conformational change required to assemble the face-centred cubic architecture, a suite of intramolecular structural parameters were calculated (Table 2). The metalloligand secondary bonding axes (2BA) angles (Figure 4a), attempts to analyse the spread between tripodal ligand arms. The metalloligand secondary bonding axis was defined by the distal pyridyl N donor and the C opposite it in the pyridyl ring. In a perfect face-centred cubic cage structure where a tripodal metalloligand occupies the corners and connects to other metalloligands through coordination to a secondary metal on the face, any angles between two adjacent facial centres connected by a shared metalloligand would be approximately 60 ˚. Small deviations of the ligand arm's direction of approach towards the Ni centre being misaligned relative to the Fe-Ni axis, allow some variations from the ideal value of 60 ˚. Next, the torsion angles arising in the pseudo C_3 axis between the coordinating imine N and the secondary pyridyl N on the same ligand arm (Figure 4b and c), which accounts for degree of twist within the

metalloligand units occupying the cage corners. The torsion angle about the pseudo C_3 axis (Figure 4b and c), between the four points including the coordinating N_{imine}, the secondary pyridyl-N on the same ligand arm, the centroid taken from the three distal pyridyl-N positions with the pseudo-C_3 Fe centre, as well as the Fe centre itself, in the order N_{imine}-Fe-centroid-$N_{pyridine}$. This torsion angle value demonstrates the degree of twist exhibited by the metalloligand itself, as well as when bound in the cage.

The average secondary bonding axes angles obtained for the metalloligand structure was 55.3 ˚, compared to 61.3 ˚ for $[Fe_8Pd_6\mathbf{L}_8]^{28+}$ (100 K only) and 61.1˚ for **1** at 275 K. This demonstrates that the angles between ligand arms for both $[Fe_8Pd_6\mathbf{L}_8]^{28+}$ and **1** HS structures must spread apart to accommodate binding to the secondary metal ion, and must do so to an almost identical extent. On the other hand, at 100 K the bond axes values of 1 increase to an average angle of 64.0˚. As such, for the metalloligand units of **1** to exhibit the LS state, they require the ability to obtain a greater angular spread. The values of torsion angles in the metalloligand were calculated to be an average of 50.1 ˚. In contrast, upon formation of the $[Fe_8Pd_6\mathbf{L}_8]^{28+}$ cage and **1** at 275 K (the HS structure) this value increased to 55.4 ˚. This shows that in both HS cage structures the degree of metalloligand twist must increase by 10.6% when forming the face-centred cubic architecture compared to that of the unbound metalloligand. However, once the spin-state of the system changes to LS Fe(II), the degree of twist becomes substantially higher, and the average torsion angle measured for the structure of **1** at 100 K was 63.2˚. This represents a 13.9% increase compared to the HS structure of **1** at 275 K. It can be seen that in order to coordinate a secondary metal, the ligand arms of the metalloligands must move away from one another and undergo a large twist. To facilitate SCO within these structures, more drastic conformational movements

within the ligand arms of the metalloligand (both the degree of twist and ligand arms moving further apart from each other) must be allowed.

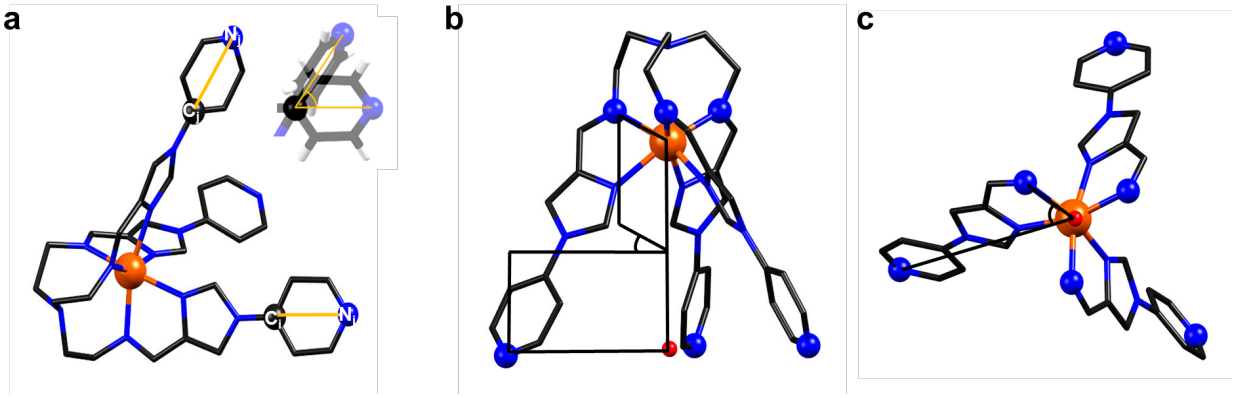

Figure 4. Schematics demonstrating the structural parameters used to quantify the degree of twist and mutual spread experienced by the secondary donor groups. a) Mutual secondary bond axes between pyridine groups. C atoms from each pair are superimposed over each other, and the angle between bonding axes is measured directly. b) Planes defined by the two sets of coordinates used in the torsion angle [N_{imine}-Fe-centroid] and [Fe-centroid-$N_{pyridine}$]. c) Torsion angle [N_{imine}-Fe-centroid-$N_{pyridine}$] as viewed along the pseudo-threefold axis, defined by the Fe-centroid interval.

Furthermore, inspection of the intramolecular distances between metal centres (Table 1) demonstrates the manner with which the cage shrinks and expands with SCO. The average Fe···Fe corner-to-opposite-corner distance (along the pseudo three-fold symmetry axis of the cage) for the HS $[Fe_8Pd_6\mathbf{L}_8]^{28+}$ cage was 25.21 Å, in comparison to 25.57 Å for the HS structure of **1** at 275 K, indicating little difference. As the temperature is decreased to 100 K in **1**, this distance decreases from 25.57 to 24.86 Å in the LS structure. On the other hand, the average Ni···Ni distance from face-to-opposite-face along the pseudo four-fold symmetry axis for **1** in its HS configuration was observed to be 16.80 Å at 275 K, which again is similar to analogous Pd···Pd distance of 16.30 Å. In the LS state of **1** (100 K), this distance increased to 17.25 Å. Therefore, the Fe···Fe and Ni···Ni

distances are, firstly, longer in the HS Ni(II) containing **1** than the $[Fe_8Pd_6\mathbf{L}_8]^{28+}$ analogue, suggesting that Pd(II) occupying the face contracts the structure inwards. Secondly, upon SCO the cage must contract along the Fe···Fe (corner-to-opposite-corner distance) three fold axis of the cage, while lastly, the Ni···Ni distance (face-to-opposite-face) must increase. This is indicating that the structure must contract along the corners and expand along the faces to facilitate SCO. Interestingly, as described above, the octahedral distortion parameters (Σ and Θ) of the Fe(II) centres increase drastically from the metalloligand in order to form $[Fe_8Pd_6\mathbf{L}_8]^{28+}$ (Table 1), while upon formation of **1** they remain very similar to the metalloligand. In contrast, they must decrease dramatically to form the LS structure. Therefore, while the arms of the metalloigand must separate and twist further to reach the LS state, and the cage must contract down the three fold axis and expand outward along the faces, it may be the effect of the Pd(II) centre on the octahedral environment of the Fe(II) centres, increasing both Σ and Θ dramatically, that that causes significant intramolecular strain throughout the cage and prevents these necessary structural reorientations explored above within the $[Fe_8Pd_6\mathbf{L}_8]^{28+}$ cage.

Another possible contributing factor for the onset of SCO in **1**, upon the introduction of Ni to the cubic face, may be intermolecular in nature. A stark difference in the structures of **1** and $[Fe_8Pd_6\mathbf{L}_8]^{28+}$ cage is the nature with which the cages pack in three dimensions. As can be seen in Figure 5a), both *Λ Λ Λ Λ Λ Λ Λ Λ* or *Δ Δ Δ Δ Δ Δ Δ Δ* homochiral enantiomers in $[Fe_8Pd_6\mathbf{L}_8]^{28+}$ pack in a very close nature, with the cages arranged face-to-face across mirror planes. The Pd(II) centres are positioned opposite one another on adjacent cages, separated by 6.9 Å, although from the BF_4^- anions that could be well resolved, it was observed that many of these counter ions occupy this space between cages faces, providing very little spacing. Similarly the Fe(II) corners are directly adjacent and are separated by 8.6 Å. The solvent accessible volume calculated with a probe

radius of 2 Å was 0.9% of the unit cell volume (Figure 5). On the other hand, the inclusion of CH_3CN bonding in the axial Ni(II) position instead causes an offset packing arrangement, where the corners of the cage pack closest to one another, nestling into the adjacent corner facilitated by CH-π interactions, and Fe(II) centres are separated by 8.9 Å, whilst the axial CH_3CN donors on the Ni(II) faces are directed towards the window of the offset adjacent cages with no appreciable intermolecular interactions. In this arrangement the nearest intermolecular Pd(II) centres are separated by 12.6 Å. The offsetting of cage packing in such as manner also produced much larger solvent accessible void spaces of 16.3 % of the unit cell volume (again using a probe with a 2 Å radius - Figure 5c). These voids are arranged throughout the spacing between the Ni(II) cage faces that results from the offset arrangement of contacting Fe(II) corners (Figure 5d). This demonstrates the conformational freedom provided to the Ni(II) faces by this packing arrangement. The closer packing of cage units is further illustrated by the crystal packing coefficient (the total percentage volume of the lattice occupied by the cage structure - see ESI for full details), where $[Fe_8Pd_6\mathbf{L}_8]^{28+}$ at 100 K displayed a value of 33.4%, meanwhile for **1** the packing coefficient decreased to 27.0 and 28.7% for **1** at 100 and 275 K respectively. This represents a decrease in the total volume of the lattice occupied by the cage molecules of 4.7% in the HS structure of **1** as compared to $[Fe_8Pd_6\mathbf{L}_8]^{28+}$, demonstrating the relative extra conformational freedom provided by the packing arrangement of **1**. As demonstrated above, a variety of intramolecular arrangements must occur with SCO, these include the expansion of the angle between tripodal metalloligand arms, twisting within these arms, opposite Fe(II) corners must pull in towards one another and opposite M(II) faces must expand away from one another. In this way the offset packing arrangement of cages in **1** may provide a smaller barrier towards these necessary molecular rearrangements, more effectively permitting SCO throughout the material.

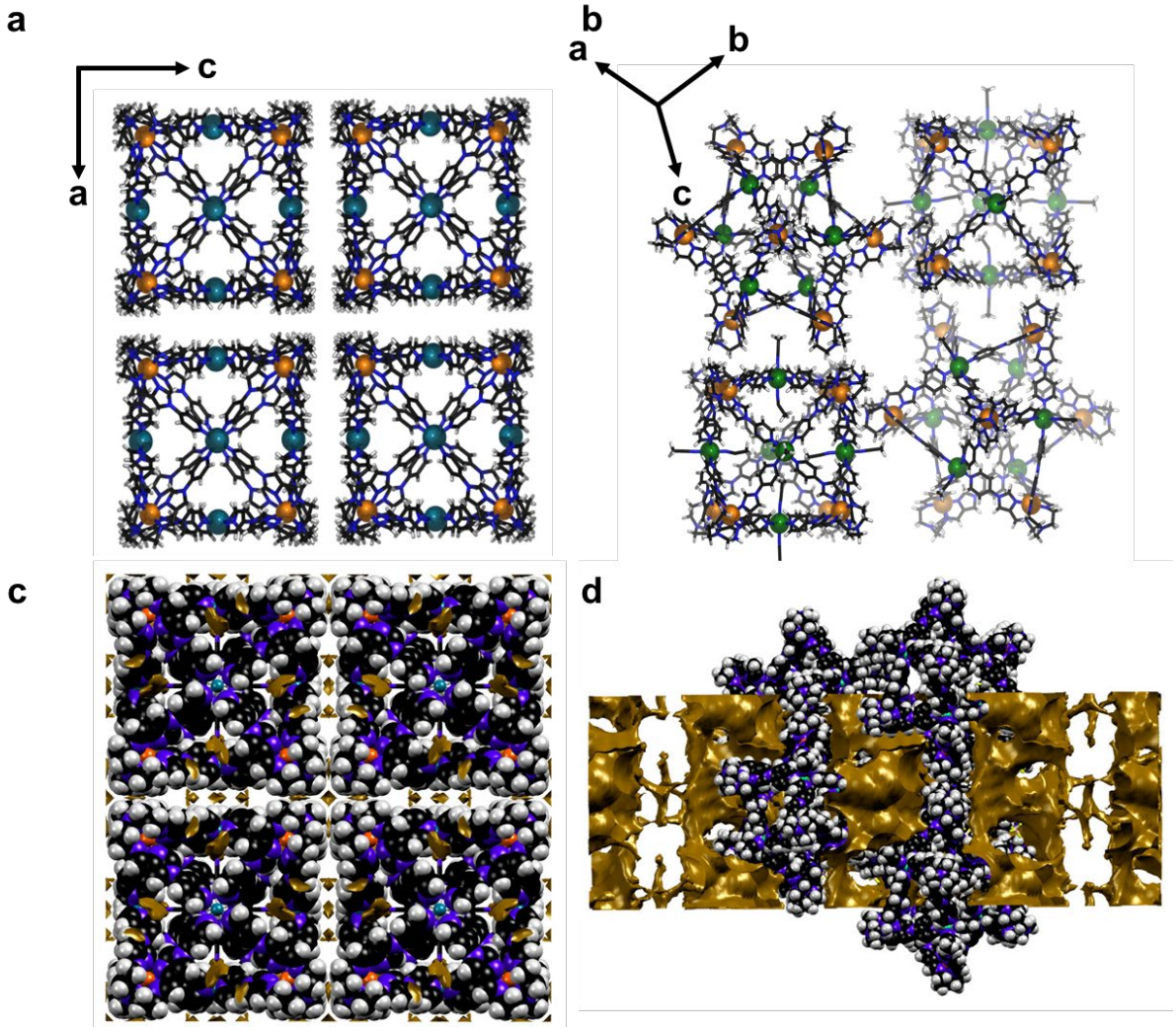

Figure 5. Schematic representation of single crystal packing of a) $[Fe_8Pd_6\mathbf{L}_8]^{28+}$ shown down the *b*-axis, b) Crystal packing of **1** viewed across the *b*-*c* plane, while c) and d) show space-filling representations of $[Fe_8Pd_6\mathbf{L}_8]^{28+}$ and **1** respectively (with atom sizes set to 0.5 times the van der Waals radius) shown with calculated solvent accessible void spaces (gold) for a probe of 2 Å radius. Both c) and d) show four cage units, and d) further shows empty white spaces to either side of the cages shown for clarity, where four more cage units would occupy. The BF_4^- anions and solvent molecules were excluded (Fe, orange; Pd, navy blue; Ni, green; C, black; N, dark blue; H, white).

Conclusion

In this report, we present a new $[Fe_8Ni_6\mathbf{L}_8(CH_3CN)_{12}]^{28+}$ heterobimetallic cage **1** exhibiting SCO. In contrast, the previously reported $[Fe_8Pd_6\mathbf{L}_8]^{28+}$ analogue, differing by the identity of the linker metal species occupying the faces of the cage, remained HS at 100 K. Magnetic susceptibility measurements demonstrated that **1** exhibited gradual, two-step, incomplete spin transition, whereby three of the eight Fe(II) metal centers underwent SCO. Mössbauer experiments at 78 K displayed area ratios of the Mössbauer absorption intensities of HS and LS species of approximately 68:32, supporting the magnetic susceptibility results. A notable LIESST effect was observed in **1** for both green and red light, with the excitation of approximately two Fe(II) centres. In contrast the VT-SCXRD experiment identified that **1** undergoes complete spin transition whereby the metalloligand corners of the cage demonstrate a change in average Fe-N bond length from 2.17 (275 K) to 1.97 Å (100 K). Through a combination of magnetic susceptibility and VT-SCXRD, it was proposed that a combined effect of inter- and intramolecular mechanisms may allow the $[Fe_8Ni_6\mathbf{L}_8(CH_3CN)_{12}]^{28+}$ structure to undergo SCO. The distorted octahedral coordination environment of the Ni(II) centre may permit more effective confirmation of the semi-rigid metalloigands upon SCO, relative to the square planar Pd(II) coordination sphere. Furthermore, the presence of axially coordinated acetonitriles force the $[Fe_8Ni_6\mathbf{L}_8(CH_3CN)_{12}]^{28+}$ cages to pack in a more offset manner compared to the close packing of the Pd(II) structure, providing further conformational freedom. This was evidenced by the packing coefficient moving from 33.4 to 28.7% in the Pd and Ni structures respectively and an increase in solvent accessible voids from 0.3 to 16.9%. These results highlight the crucial role of the identity of the secondary metal and its axial donors, in this case occupying the faces of the cubic cage, on the overall ability of the architecture to undergo intramolecular rearrangements and in permitting SCO. Design through selectivity of secondary metal centres effect on the conformational ability of the

metalloligand units and the effect of axial donors on packing arrangements may serve as new routes in the engineering of SCO or non-SCO cage systems and may inform the future design of multifunctional heteronuclear coordination cages possessing SCO capabilities.

Materials and Methods

Physical Measurements

Simultaneous thermal analysis (STA) experiment was carried out on a NETZSCH STA-449 Jupiter Instrument. STA measurements were acquired using Nitrogen for both the purge and protective gases; sample was weighed into an aluminium crucible and measurements were collected from a temperature range of 303 to 863 K at a rate of 10 K/min.

Scanning Electron Microscopy (SEM) and Energy Dispersive Spectroscopy (EDS) spot analysis and X-ray mapping were acquired using a Phenom XL in low vacuum with a chamber pressure of 10 Pa and accelerating voltage of 15kV. All samples were mounted to an aluminium stub with double-sided conductive carbon tape and silicon wafers, images were taken uncoated. Spot EDS and X-ray mapping analysis was carried out using Phenom EDS software with a silicon drift detector (SDD).

Susceptibility data were collected using a Quantum Design SQUID magnetometer calibrated against a standard palladium sample. Single crystals were filtered from diffusion vials before air drying. Magnetic susceptibility measurements were collected between 5 K to 400 K at scan rates of 1 and 4 K/min in cooling and heating modes. The sample was held at 400 K for 60 minutes to allow desolvation to take place, cooling and heating runs were collected for the desolvated sample from 400 K to 5 K to 400 K at scan rates of 1 and 4 K min^{-1}. Measurements were taken continuously under an applied field of 0.5 T.

Mössbauer experiments were conducted on a Wissel MVT-1000 Mössbauer spectrometer with a ^{57}Co/Rh source in a constant-acceleration transmission spectrometer (Topologic Systems) equipped with a closed-cycle helium refrigerator cryostat (Iwatani Co., Ltd.). All isomer shifts are given relative to α-Fe at room temperature.

Synthesis of cage 1. Nickel (II) tetrafluoroborate hexahydrate (107.8 mg, 0.31 mol) in 20 mL of CH_3CN was added dropwise to a solution of Fe**L**$(BF_4)_2$ (353.8 mg, 0.42 mol) in 10 mL of CH_3CN. The reaction mixture was heated to reflux with stirring for 1 h under nitrogen atmosphere. The resulting orange solution was slowly diffused in di-isopropyl ether which resulted in the formation of dark red/orange crystals. The crystals were then filtered and air dried to give dark red/orange crystal of **1.** Yield: 259 mg, 57.0%. Elemental analysis (%) calculated, measured for **1**+ 59 H_2O): C (34.52, 34.64), H (4.86, 4.83), N (15.86, 15.73); Due to the quick decay of crystal after losing solvent from SEM image, powder X-ray diffraction experiments could not be conducted.

Single crystal X-ray Diffraction measurements.

Single crystal data for **1** were collected from the MX1 beamline at the Australian Synchrotron, using silicon double crystal chromated radiation (λ = 0.71073 Å) at 100, 150, 200, 250 and 275 K.[58] The single crystal data at 300 K could not be collected as the crystallinity started to wane off beyond 275 K, resulting in loss of diffraction. At the Australian synchrotron beamline, the XDS software[59] was used for data integration, processing and scaling. The empirical absorption correction was then applied at the synchrotron using SADABS.[60] The structure was solved by ShelXT[61] using a suite of SHELX programs[62-63] via the Olex2 interface[64]. Non-hydorgen atoms were refined anisotropically for heterometallic cage **1** and hydrogen atoms were included in idealised position and refined using a riding model. The crystallographic data in CIF format has

been deposited at the Cambridge Crystallographic Data Centre with CCDC number 2194121-2194125. The CIF is available free of charge from the Cambridge Crystallographic Data Centre, 12 Union Road, Cambridge CB2 1 EZ, UK; fax: (+44) 1223-336-033; or email: deposit@ccdc.cam.ac.uk. Crystals of heterometallic cage **1** diffracted only to lower angles of theta and therefore the data for **1** was collected at low resolution (~1.06Å). Structure of **1** at 100 and 150 K there are a total of five BF_4^- anions seen outside the cage with four BF_4^- anions present in the 200 K structure. Despite numerous attempts at modelling anions and solvents in the crystal lattice at 250 and 275 K, together with the low resolution (1.06 Å) and the thermal motion and disorder, the electron density of solvents and anions associated with them could not be found in the crystal lattice.

The non-hydrogen atoms of **1** at all temperatures were refined anistropically with hydrogen atoms included in idealized positions and refined using a riding model. For all temperatures of **1**, the obtained geometry from the metalloligand was used to refine the atoms of the ligand. Restraints like RIGU and DFIX were used in the pyridyl, imidazole, Tren (Tris(2-aminoethyl)amine) groups and the coordinating CH_3CN of the cage and SADI ,RIGU and DFIX were used for the BF_4^- anions at lower temperatures. Solvent mask was applied to all temperatures of **1**, which found residual electron densities of 2820, 2870, 2876, 2696 and 2532 at 100, 150, 200, 250 and 275 K respectively. The final R factors are in the range of (~0.12-0.14) with wR2 and GooF values in acceptable ranges for this large asymmetric unit in the monoclinic space group.

ASSOCIATED CONTENT

The Supporting Information is available free of charge on the ACS Publications website at DOI:. CCDC 2194121 - 2194125 contain the supplementary crystallographic data for this paper. These data can be obtained free of charge via www.ccdc.cam.ac.uk, or by emailing data_request@ccdc.cam.ac.uk, or by contracting The cambridge Crystallographic Data Center, 12 Union Road, Cambridge CB2 1EZ, UK; fax: + 44 1223 336033.

Physical measurements, crystallographic tables of complex, calculation of crystallographic parameters and magnetic susceptibility data, including Figures S1-S4 and Table S1 (PDF)

X-ray crystallographic data for **1** at 100 K (CIF)

X-ray crystallographic data for **1** at 150 K (CIF)

X-ray crystallographic data for **1** at 200 K (CIF)

X-ray crystallographic data for **1** at 250 K (CIF)

X-ray crystallographic data for **1** at 275 K (CIF)

AUTHOR INFORMATION

Corresponding Author

Feng Li - *School of Science, Western Sydney University, Locked Bag 1797, Penrith NSW 2751, Australia*; Email: feng.li@westernsydney.edu.au

Authors

Hyunsung Min - *School of Science, Western Sydney University, Locked Bag 1797, Penrith NSW 2751, Australia*

Alexander R. Craze - *School of Science, Western Sydney University, Locked Bag 1797, Penrith NSW 2751, Australia*

Matthew J. Wallis - *School of Science, Western Sydney University, Locked Bag 1797, Penrith NSW 2751, Australia*

Ryuya Tokunaga - *Department of Chemistry, Graduate School of Science and Technology, Kumamoto University, 2-39-1 Kurokami, Chuo-ku, Kumamoto 860-8555, Japan*

Takahiro Taira - *Department of Chemistry, Graduate School of Science and Technology, Kumamoto University, 2-39-1 Kurokami, Chuo-ku, Kumamoto 860-8555, Japan*

Yutaka Hirai - *Department of Chemistry, Graduate School of Science and Technology, Kumamoto University, 2-39-1 Kurokami, Chuo-ku, Kumamoto 860-8555, Japan*

Mohan M. Bhadbhade - *Mark Wainwright Analytical Centre, University of New South Wales, Kensington, NSW, 2052, Australia*

Daniel J. Fanna - *Advanced materials Characterisation Facility, Western Sydney University, Locked Bag 1797, Penrith NSW 2751, Australia*

Christopher E. Marjo - *Mark Wainwright Analytical Centre, University of New South Wales, Kensington, NSW, 2052, Australia*

Shinya Hayami - *Department of Chemistry, Graduate School of Science and Technology, Kumamoto University, 2-39-1 Kurokami, Chuo-ku, Kumamoto 860-8555, Japan*

Leonard F. Lindoy - *School of Chemistry F11, The University of Sydney, NSW 2006, Australia*

Present Addresses

†**Alexander R. Craze -** *Department of Chemistry, University of Oxford, 12 Mansfield Road, Oxford OX1 3TA, UK*

Author Contributions

Funding Sources

This research received no external funding.

Notes

Any additional relevant notes should be placed here.

ACKNOWLEDGMENT

The authors would like to thank Western Sydney University (WSU) for research funding, the Advanced Materials Characterisation Facility (AMCF) at WSU, Mark Wainwright Analytical Centre at UNSW and Kumamoto University at which the magnetic susceptibility and Mössbauer experiments were conducted. The crystallographic data were performed on the MX1 beamline of the Australian Synchrotron, Clayton, Victoria, Australia. We also thank the Australian Synchrotron for the travel support and their staff for beamline assistance.

References

1 McConnell, A. J. *Chem. Soc. Rev.* **2022**, *51*, 2957-2971, 10.1039/D1CS01143J.

2 McTernan, C. T.; Davies, J. A.; Nitschke, J. R. *Chem. Rev.* **2022**, *122*, 10393-10437, 10.1021/acs.chemrev.1c00763.

3 Ning X.; Tan Y-X.; El-Sayed, E.-S. M. *Cryst. Growth Des.* **2022**, *22*, 2768-2773, 10.1021/acs.cgd.2c00243.

4 Li, W.; Li, S.; Liu, C.; Rotaru, A.; Robeyns, K.; Singleton, M. L.; Garcia, Y. *J. Mater. Chem. C.* **2022**, *10,* 9216-9221, DOI: 10.1039/d2tc01655a.

5 Li, Y-W.; Li, J.; Wan, X-Y.; Shen, D-F.; Yan, H.; Zhang, S-S.; Ma, H-Y.; Wang, S-N.; Li, D-C.; Gao, Z-Y.; Dou, J-M.; Sun, Di. *Inorg. Chem.* **2021**, *60*, 671-681, https://dx.doi.org/10.1021/acs.inorgchem.0c02629.

6 Zhang, Z.; Zhao, Z.; Wu, L.; Lu, S.; Ling, S.; Li, G.; Xu, L.; Ma, L.; Hou, Y.; Wang, X.; Li, X.; He, G.; Wang, K.; Zou, B.; Zhang, M. *J. Am. Chem. Soc.* **2020**, *142*, 2592-2600, 10.1021/jacs.9b12689.

7 Lu, Y-L.; Song, J-Q.; Qin, Y-H.; Guo, J.; Huang, Y-H.; Zhang, X-D.; Pan, M.; Su, C-Y. *J. Am. Chem. Soc.* **2022**, 144, 8778-8788, 10.1021/jacs.2c02692.

8 Xue, Y.; Hang, X.; Ding, J.; Li, B.; Zhu, R.; Pang, H.; Xu, Q. *Coord. Chem. Rev.* **2021**, *430*, 213656, 10.1016/j.ccr.2020.213656.

Tan, C.; Chu, D.; Tang, X.; Liu, Y.; Xuan, W.; Cui, Y. *Chem. Eur. J.* **2019**, *25*, 662-672, 10.1002/chem.201802817.

10 Gao, W-X.; Zhang, H-N.; Jin, G-X. *Coord. Chem. Rev.* **2019**, *386*, 69-84, 10.1016/j.ccr.2019.01.023.

11 Preston, D.; Lewis, J. E. M.; Crowley, J. D. *J. Am. Chem. Soc.* **2017**, *139*, 2379-2386, 10.1021/jacs.6b11982.

12 Zhen, Y-R.; Suntharalingam, K.; Johnstone, T. C.; Lippard, S. J. *Chem. Sci.* **2015**, *6*, 1189-1193, 10.1039/C4SC01892C.

13 Zhu, C.; Yang, K.; Wang, H.; Fang, Y.; Feng, L.; Zhang, J.; Xiao, Z.; Wu, X.; Li, Y.; Fu, Y.; Zhang, W.; Wang, K-Y.; Zhou, H-C. *ACS Cent. Sci.* **2022**, *8*, 562-570, 10.1021/acscentsci.1c01571.

14 Zhang, D.; Ronson, T. K.; Zou, Y-Q.; Nitschke, J. R. *Nat. Rev. Chem.* **2021**, *5*, 168-182, 10.1038/s41570-020-00246-1.

15 Jackson, G. D.; Tipping, M. B.; Taylor, C. G. P.; Piper, J. R.; Pritchard, C.; Mozaceanu, C.; Ward. M. D. *Chemistry*, **2021**, *3*, 1203-1214, 10.3390/chemistry3040088.

16 Yadav, S.; Kannan, P.; Qiu, G. *Org. Chem. Front.* **2020**, *7*, 2842-2872, 10.1039/D0QO00681E.

17 Brzechwa-Chodzyńska, A.; Drożdż, W.; Harrowfield, J.; Stefankiewicz, A. R. *Coord. Chem. Rev.* **2021**, *434*, 213820, 10.1016/j.ccr.2021.213820.

18 Hu, X.; Han, M.; Shao, L.; Zhang, C.; Zhang, L.; Kelley, S. P.; Zhang, C.; Lin, J.; Dalgarno, S. J.; Atwood, D. A.; Feng S.; Atwood, J. L. *Angew. Chem. Int. Ed.* **2021**, *60*, 10516-10520, 10.1002/anie.202016077.

19 Wezenber, S. J. *Chem. Lett.* **2020**, *49*, 609-615, 10.1246/cl.200076.

20 Hardy, M.; Lützen, A. *Chem. Eur. J.* **2020**, *26*, 13332-13346, 10.1002/chem.202001602.

21 McConnell, A. J. *Supramolecular Chemistry*, **2018**, *30*, 858-868, 10.1080/10610278.2017.1406093.

22 Glatz, J.; Chamoreau, L-M.; Flambard, A.; Meunier, J-F.; Bousseksou, A.; Lescouëzec, R. *Chem. Commun.* **2020**, 56, 10950-10953, DOI: 10.1039/d0cc04279j.

23 Hardy, M.; Tessarolo, J.; Holstein, J. J.; Struch, N.; Wagner, N.; Weisbarth, R.; Engeser, M.; Beck, J.; Horiuchi, S.; Clever, G. H.; Lützen, A. *Angew. Chem. Int. Ed.* **2021**, *60*, 22562-22569, 10.1002/anie.202108792.

24 Berdiell, I. C.; Hochdörffer, T.; Desplanches, C.; Kulmaczewski, R.; Shahid, N.; Wolny, J. A.; Warriner, S. L.; Cespedes, O.; Schünemann, Chastanet, G.; Halcrow, M. A. *J. Am. Chem. Soc.* **2019**, *141,* 18759-18770, 10.1021/jacs.9b08862.

25 Zhang, F-L.; Chen, J-Q.; Qin, L-F.; Tian, L.; Li, Z.; Ren, X.; Gu, Z-G. *Chem. Commun.* **2016**, *52*, 4796-4799, 10.1039/C6CC00711B.

26 Li, L.; Saigo, N.; Zhang, Y.; Fanna, D. J.; Shepherd, N. D.; Clegg, J. K.; Zheng, R.; Hayami, S.; Lindoy, L. F.; Aldrich-Wright, J. R.; Li, C-G.; Reynolds, J. K.; Harman, D. G.; Li, F. *J. Mater. Chem. C.* **2015**, *3*, 7878-7882, 10.1039/C5TC00991J.

27 Li, L.; Craze, A. R.; Mustonen, O.; Zenno, H.; Whittaker, J. J.; Hayami, S.; Lindoy, L. F.; Marjo, C. E.; Clegg, J. K.; Aldrich-Wright, J. R.; Li, F. *Dalton Trans.* **2019**, *48*, 9935-9938, 10.1039/C9DT01947B.

28 Howard-Smith, k. J.; Craze, A. R.; Zenno, G.; Yagyu, J.; Hayami, S.; Li, F. *Chem. Commun.* **2020**, *56*, 8838-8841, 10.1039/D0CC03708G.

29 Craze, A. R.; Bhadbhade, M. M.; Komatsumaru, Y.; Marjo, C. E.; Hayami, S.; Li, F. *Inorg. Chem.* **2020**, *59*, 1274-1283, 10.1021/acs.inorgchem.9b02995.

30 Craze, A. R.; Sciortino, N. F.; Bhadbhade, M. M.; Kepert, C. J.; Marjo, C. E.; Li, F. *Inorganics*, **2017**, *5*, 62, 10.3390/inorganics5040062.

31 Craze, A. R.; Bhadbhade, M. M.; Kepert, C. J.; Lindoy, L. F.; Marjo, C. E.; Li, F. *Crystals*, **2018**, *8,* 376, 10.3390/cryst8100376.

32 Li, L.; Neville, S. M.; Craze, A. R.; Clegg, J. k.; Sciortino, N. F.; Athukorala Arachchige, K. S.; Mustonen, O.; Marjo, C. E..; McRae, C. R.; Kepert, C. J.; Lindoy, L. F.; Aldrich-Wright, J. R.; Li, F. *ACS Omega.* **2017**, *2*, 3349-3353, 10.1021/acsomega.7b00630.

33 Craze, A. R.; Howard-S,ith, K. J.; Bhadbhade, M. M.; Mustonen, O.; Kepert, C. J.; Marjo, C . E.; Li, F. *Inorg. Chem.* **2018**, *57*, 6503-6510, 10.1021/acs.inorgchem.8b00576.

34 Hogue, R. W.; Singh, S.; Brooker, S. *Chem. Soc. Rev.* **2018**, *47*, 7303-7338, 10.1039/C7CS00835J.

35 Ren, D-H.; Qiu, D.; Pang, C-Y.; Li, Z.; Gu, Z-G. *Chem. Commun.* **2015**, *51*, 788-791, 10.1039/C4CC08041F.

36 Ferguson, A.; Squire, M. A.; Siretanu, D.; Mitcov, D.; Mathonière, C.; Clérac, R.; Kruger, P. E. *Chem. Comm.* **2013**, *49,* 1597-1599, 10.1039/c3cc00012e.

37 Bilbeisi, R. A.; Zarra, S.; Feltham, H. L. C.; Jameson, G. N. L.; Clegg, J. K.; Brooker, S.; Nitschke, J. R. *Chem. Eur. J.* **2013**, *19*, 8058-8062, 10.1002/chem.201300805.

38 Struch, N.; Bannwarth, C.; Ronson, T. K.; Lorenz, Y.; Mienert, B.; Wagner, N.; Engeser, M.; Bill, E.; Puttreddy, R.; Rissanen, K.; Beck, J.; Grimme, S.; Nitschke, J. R.; Lützen, A. *Angew. Chem. Int. Ed.* **2017**, *56*, 4930-4935. DOI:10.1002/anie.20170083.

39 Duriska, M. B.; Neville, S. M.; Moubaraki, B.; Cashion, J. D.; halder, G. J.; Chapman, K. W.; Balde, C.; Létard, J-F.; Murray, K. S.; Kepert, C. J.; Batten, S. R. *Angew. Chem.* **2009**, *121*, 2587-2590. DOI: 10.1002/ange.200805178.

40 Duriska, M. B.; Neville, S. M.; Moubaraki,; Murray, K. S.; Balde, C.; Létard, J-F.; Kepert, C. J.; Batten, S. R. *ChemPlusChem.* **2012**, *77*, 616-623. DOI: 10.1002/cplu.201200123.

41 Lu, H-S.; Han, W-K.; Yan, X.; Xu, Y-X.; Zhang, H-X.; Li, T.; Gong, Y.; Hu, Q-T.; Gu, Z-G. *Dalton Trans.* **2020**, *49*, 4420-4224. DOI: 10.1039/d0dt00353k.

42 Berdiell, I. C.; Hochdörffer.; Desplanches, C.; Kulmaczewski, R.; Shahid, N.; Wolny, J. A.; Warriner, S. L.; Cespedes, O.; Schünemann, V.; Chastanet, G.; Halcrow, M. A. *J. Am. Chem. Soc.* **2019**, *141*, 18759-18770. DOI: 10.1021/jacs.9b08862.

43 Zhang, D.; Ronson, T. K.; Nitschke, J. R. *Acc. Chem. Res.* **2018**, *51*, 2423-2436, 10.1021/acs.accounts.8b00303.

44 Cook. T. R.; Stang, p. J. *Chem. Rev.* **2015**, *115*, 7001-7045, 10.1021/cr5005666.

45 Fujita, m.; Umemoto, K.; Yoshizawa, M.; Fujita, N.; Kusukawa,T.; Biradha, K. *Chem. Commun.* **2001**, 509-518. DOI: 10.1039/b008684n.

46 Zhou, X-C.; Wu, L-X.; Wang, X-Z.; Lai, Y-L.; Ge, Y-Y.; Su, J.; Zhou, X-P.; Li D. *Inorg. Chem.* **2022**, *61*, 5196-5200, 10.1021/acs.inorgchem.2c00283.

47 Min, H.; Craze, A.; Tairo, T.; Wallis, M. J.; Bhadbhade, M. M.; Tian, R.; Fanna, D. J.; Wuhrer, R.; Hayami, S.; Clegg, J. K.; Marjo, C. E.; Lindoy, L. F.; Li, F. *Chemistry*, **2022**, *4*, 535, 10.3390/chemistry4020038.

48 Sudan, S.; Li, R-J.; Jansze, S. M.; Platzek, A.; Rudolf, R.; Clever, G. H.; Fadaei-Tirani, F.; Scopelliti, R.; Severin, K. *J. Am. Chem. Soc.* **2021**, *143*, 1773-1778, 10.1021/jacs.0c12793.

49 Hardy, M.; Struch, N.; Topić, F.; Schnakenburg, G.; Rissanen, K.; Lützen, A. *Inorg. Chem.* **2018**, *57*, 3507-3515, DOI: 10.1021/acs.inorgchem.7b02516.

50 Zhang, Y-Y.; Gao, W-X.l Lin, L.; Jin, G-X. *Coord. Chem. Rev.* **2017**, *344*, 323-344, 10.1016/j.ccr.2016.09.010.

51 Li, L.; Fanna, D. J.; Shepherd, N. D.; Lindoy, L. F.; Li, F. *J. Incl. Phenom. Macrocycl. Chem.* **2015**, *82*, 3-12, 10.1007/s10847-015-0520-0.

52 Li, L.; Zhang, Y.; Avdeev, M.; Lindoy, L. F., Harman D. G.; Zhen, R.; Cheng, Z.; Aldrich-Wright, J. R.; Li, F. *Dalton Trans*. **2016**, *45*, 9407-9411, DOI: 10.1039/c6dt01651k

53 Li, F.; Lindoy, L. F. *Aust. J. Chem.* **2019**, *72*, 731, 10.1071/CH19279.

54 Reichel, F.; Clegg, J. K.; Gloe, K.; Gloe, K.; Weigand, J. J.; Reynolds, J. K.; Li, C-G.; Aldrich-Wright, J. R.; Kepert, C. J.; Lindoy, L. F.; Yao, H-C.; Li, F. *Inorg. Chem.* **2014**, *53*, 688-690, 10.1021/ic402686s.

55 Pullen, S.; Tessarolo, J.; Clever, G. H. *Chem. Sci.* **2021**, *12*, 7269-7293, 10.1039/D1SC01226F.

56 Ketkaew, R.; Tantirungrotechai, Y.; Harding, D.J.; Harding, P.; Chastanet, G.; Guionneau, P.; Marchivie, M. *Dalton Trans.* **2021**, *50*, 1086-1096.

57 Schmitz, S.; Leusen, J. V.; Ellern, A.; Kögerler, P.; Monakhov, K. Y. *Inorg. Chem. Front.* **2016**, *3*, 523-531.

58 Cowieson, N.P.; Aragao, D.; Clift, M.; Ericsson, D.J.; Gee, C.; Harrop, S.J.; Mudie, N.; Panjikar, S.; Price, J.R.; Riboldi-Tunnicliffe, A.; et al. MX1: A bending-magnet crystallography beamline serving both chemical and macromolecular crystallography communities at the Australian Synchrotron. *J. Synchrotron Rad.* **2015**, 22, 187–190.

59 Kabsch, W. XDS. Automatic processing of rotation diffraction data from crystals of initially unknown symmetry and cell constants. *J. Appl. Crystallogr.* **1993**, 26, 795–800.

60 SADABS, version 2014/5; Bruker AXS Inc.: Madison, WI, USA, **2001**.

61 Sheldrick, G.M. SHELXT—Integrated space-group and crystal-structure determination. Acta. Cryst. A **2015**, 71, 3–8.

62 Sheldrick, G.M. SHELX-2014: Programs for Crystal Structure Analysis; University of Göttingen: Göttingen, Lower Saxony, Germany, **2014**.

63 Sheldrick, G.M. Crystal structure refinement with SHELXL. *Acta. Cryst. C.* **2015**, 71, 3–8.

64 Dolomanov, O.V.; Bourhis, L.J.; Gildea, R.J.; Howard, J.A.K.; Puschmann, H. OLEX2: A complete structure solution, refinement and analysis program. *J. Appl. Cryst.* **2009**, 42, 339–341.